1

Aluminum Alloys: Fundamentals of Welding Metallurgy

1.1 Introduction

Aluminum (Al) alloys have been used traditionally for structural parts of aircrafts. At the beginning of the twenty-first century, the leading aircraft companies started to use composite materials due to their advantages such as low weight. Nonetheless, the usage of Al in structural parts still continues due to better recyclability of these materials and satisfying the weight reduction of the structure [1]. Al is a light alloy with a density of 2.7 g/cm^3, is nonmagnetic, has an FCC crystal structure, has high formability and low-temperature toughness, and has a relatively high corrosion resistance depending on the alloying elements [2]. Al alloys are also easily processible with casting, machining, and extrusion. Some Al alloys capable of precipitation hardening have strengths comparable to steels [2]. In contrast to carbon and low-alloy steels, Al does not possess any polymorph; therefore, only the solidification behavior determines the properties of the weld zone in the fusion welding [3]. Cooling of the solidified weld zone does not have a prominent effect on the microstructure of the weld due to absence of any polymorph transformation in Al alloys.

Al alloys are classified based on their mechanical properties, manufacturing process, and alloying elements. Wrought Al alloys are determined by the degree of cold work and chemical composition. Cast Al alloys are determined by the casting process and chemical composition. Other mechanisms such as precipitation hardening and solid-solution hardening may also contribute to the strength of Al alloys [2]. The alloying elements that promote precipitation hardening in Al are Cu, Cu—Mg, Cu—Li, Cu—Si, Zn, Zn—Mg, Zn—Mg—Cu, and Li—Cu—Mg [2]. The alloying elements that promote solid-solution hardening are Mn, Si, Zn, Mg, and Cu [2].

The designation system for wrought Al alloys in the European standard system is a four-digit numeric. Figure 1.1 shows the designation system according to the European standard. There is also a supplementary designation system whose basis is a chemical symbol. The applications of some Al alloys are provided in Table 1.1.

Along with austenitic stainless steel and Ni alloys, Al alloys are good candidates for the construction of LNG cargo containment, as Al possesses a high toughness due to its FCC structure [11]. The usage of Al alloys as structural materials requires their joining in various joint designs. Mechanical joining methods such as riveting have been used in lap configuration, which adds to the weight of the

Welding Metallurgy of Aluminium Alloys: Design, Processes, and Simulations, First Edition.
Reza Beygi, Eduardo André de Sousa Marques, Ricardo João Camilo Carbas, and Lucas Filipe Martins da Silva.

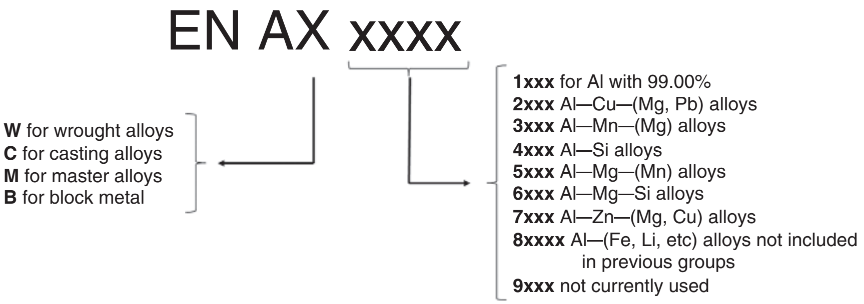

Figure 1.1 Designation system for wrought aluminum alloys according to the European standard.

Table 1.1 The applications of some Al alloys.

Alloy	**Application**
AA2xxx	Propellant cabin of launch vehicles [4]
AA5xxx	Shipbuilding [5]
AA6xxx	Car body [6], battery tray [7]
AA7xxx	Bicycle frame [8], panel structure of launcher [9], underframe in high-speed trains [10]

structure. An example is the stringer–skin connection used in the fuselage of the aircraft (Figure 1.2a), where additional adhesive is used to seal the joint. Welding technologies help to reduce the weight by eliminating the overlap region and the sealant and while maintaining the same performance (Figure 1.2b) [12]. In Tee-joining, the high heat conductivity of Al causes a high thermal gradient to form between the weld pool and base material. Lap joining also adds to the weight of the structure and hence is used for thin sheets less than 1 mm, where welding processes such as resistance welding are to be used. Regarding the weld design, fillet welds are usually avoided in the structural parts under fatigue due to crack initiation from the root of the weld [13]. The joint design also affects the residual stress during welding. For instance, the Tee-joints cause a higher residual stress during welding than lap joints due to higher heat sink effect in the Tee-joints, which causes a higher cooling rate [14].

The Al alloys that are heat-treatable (HTA) need to undergo specific sequences during forming and assembling to obtain desired mechanical properties. For example, in the car body, the Al sheets are welded in a solution-treated or hot-formed state. The final aging treatment, which is connected to the paint bake cycle, is performed after welding [15]. Figure 1.3 shows the schematic workflow of Al alloy used in the car body. Hot forming of Al alloy is performed in the solid-solution state, which is quenched subsequently to preserve the solid-solution state. The joining methods are performed after this stage, and then a paint bake cycle is carried out to regain the strength through aging treatment.

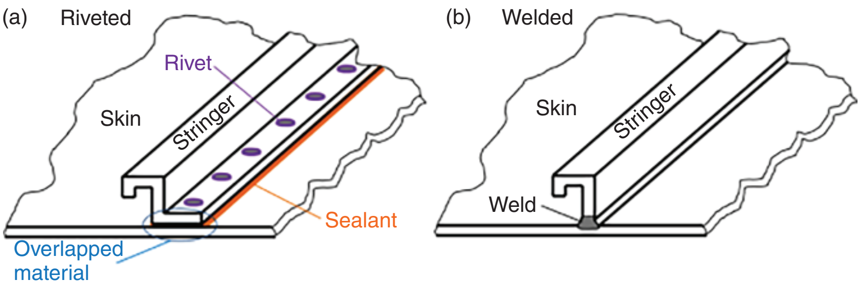

Figure 1.2 Joining of a stringer–skin aluminum part used in the fuselage of the aircraft made by (a) riveting and (b) welding. Source: Ref. [12]/with permission of Elsevier.

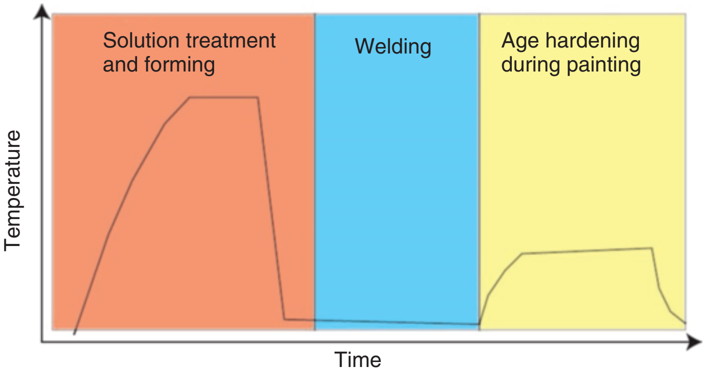

Figure 1.3 The forming, solution treatment, welding, and age hardening while paint baking of Al alloys used in the car body.

There are some challenges during welding of Al alloys, and understanding their mechanisms helps to avoid them and hence obtain the optimum performance of the welded structure. Some issues that exist during welding steel are not present during welding Al due to its physical properties. For instance, Al is a nonmagnetic material and therefore the problems of arc blowing will not occur during arc welding processes. Instead, other issues are pronounced during welding Al. The thermal conductivity of Al is six times that of steel and therefore the welding processes with high power density need to be used for Al. Though the melting point of Al is low, due to high specific heat of Al the heat sources need to have high intensity. Due to the high heat conductivity of Al, the use of welding processes with low heat intensity for wrought alloys and precipitation-hardened alloys produces a wide heat-affected zone (HAZ) with lower strength (due to softening) and distortion. In precipitation-hardened alloys, it is also probable that the precipitates in the HAZ dissolve and reprecipitate, which leads to brittleness [2]. The thermal expansion coefficient of Al is twice that of steel. This along with its low Young's modulus causes a high distortion, especially in thin structures, making it difficult to maintain the tolerances [16]. To keep the distortion within the limits of tolerance, the components need to be tightly clamped and often tack-welded. The welding sequence also needs to be planned carefully [2].

A significant difference between steel and Al arises from metallurgical aspects. Structural steels encounter phase transformation during cooling; the most important one is the austenite to ferrite transformation. While the strength of structural steels increases in the HAZ during welding, Al alloys lose their strength in the HAZ. A higher number of issues exist while welding Al alloys that are heat-treatable, which means their strength is increased by precipitation. Other Al alloys get their strength by other mechanisms such as solution hardening and work hardening. Three main series of heat-treatable Al alloys are introduced in the following.

1.1.1 Aluminum–Copper Alloys

Al—Cu alloys known as 2xxx family are mainly used in the structure of the airframes and possess high fatigue strength. The precipitation hardening is the main mechanism of strengthening in these alloys. From the supersaturated state, a series of phases form by the increase in temperature:

$$\text{Supersaturated alloy} \rightarrow \text{GPI} \rightarrow \text{GPII}(\theta') \rightarrow \theta' \rightarrow \theta\ (\text{Al}_2\text{Cu or Al}_2\text{CuMg})$$

GP phases are coherent phases and differ in the size and the lattice strain they induce. θ' and θ are semi-coherent and incoherent, respectively, the latter being the equilibrium phase, whose contribution to the strength is the lowest compared to the other phases.

1.1.2 Aluminum–Zinc–Magnesium Alloys

$MgZn_2$ is the main precipitate in this group of Al alloy. These Al alloys are less sensitive to quenching, and thus a supersaturated condition can be obtained even after air cooling. Natural aging can occur in these alloys after a couple of months to recover their initial hardness, making these alloys to have a self-hardening effect [17]. So, these alloys do not need a post-weld heat treatment (PWHT) to recover their hardness. However, these alloys are susceptible to solidification cracking (SC) in the fusion zone (FZ) and liquidation cracking in HAZ. Evaporation of Mg and Zn due to their low boiling point can cause pore formation during welding [18].

1.1.3 Aluminum–Magnesium–Silicium

The strength in the HAZ of these alloys is only partially restored by subsequent aging, as explained in Figure 1.28. The degree of strength lost in the HAZ depends on the heat and the time it receives this heat. It means that the welding process and its parameters determine the degree of strength lost in the HAZ. A lower heat input favors a narrower HAZ region that is less softened.

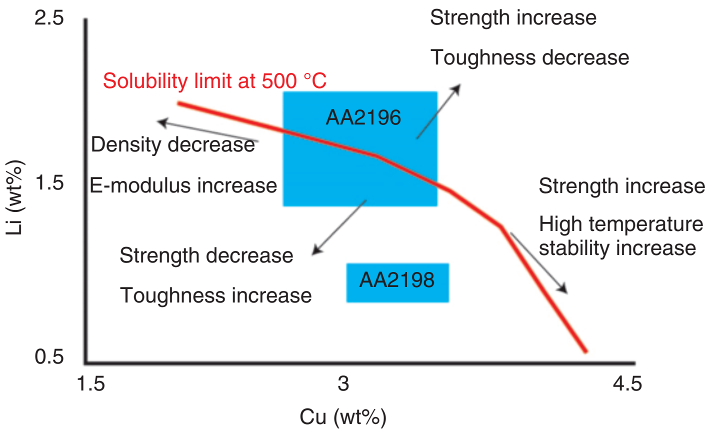

Figure 1.4 Schematic representation of mechanical properties of Al–Li–Cu alloys in relation to Cu and Li content. Source: Adapted from [19].

1.1.4 Aluminum–Lithium Alloys

These alloys, as special Al alloys, are used in the aircraft industry. Lithium has a low density and a high solubility in Al and hence offers a great potential to be used in the structure of airplanes. 1% lithium decreases the density of Al by 3% and increases the elastic modulus by 6% [19]. Some Al–Li alloys belong to Al—Cu—Li alloys such as AA2196 (found as extruded parts) and AA2198 (found as sheets and plates) [19]. The mechanical properties of these alloys primarily depend on the content of copper and lithium, as shown in Figure 1.4 [20]. The red line shows the solubility limit at 500 °C. The increase in Cu leads to an increase in Al_2CuLi precipitation hardening phases, which increase the strength. An increase in Li promotes the formation of Al_3Li precipitates and lowers the density. In addition to precipitates, the dispersoids may also exist. Dispersoids, in contrast to precipitates, are formed above the solubility limit temperature, and hence they cannot be altered by heat treatment of the solid alloy. Manganese is an element that forms incoherent dispersoids and increases the toughness and fatigue strength [19]. In Al—Mg—Li alloys, the main precipitate is Al_3Li. Al—Li alloys are prone to pore formation during welding, which downgrades their weldability [21].

1.2 Weldability

Welding of Al affects the mechanical properties due to the change in the microstructure during solidification as well as the heat effects in the solid state. The surface tension and the viscosity of the Al melt are low [22]. This increases the risk of melt burn through and spatter during welding Al. The physical, chemical, and metallurgical properties of Al alloys influence their behavior during the welding processes. Despite having a low melting temperature (up to 650 °C), a high thermal conductivity of Al ($\lambda = 120-240$ W/m K) necessitates a high heat intensity for welding.

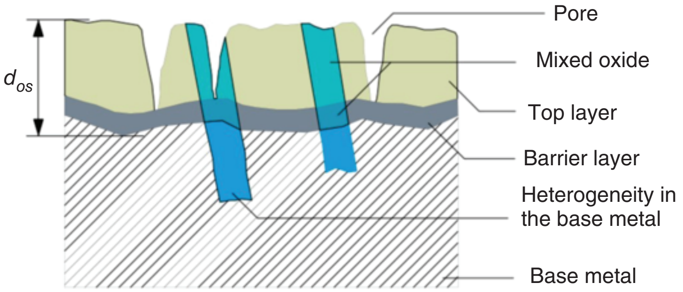

Figure 1.5 Structure of the Al oxide layer in wet air. Source: Adapted from [19].

The thermal conductivity of Al decreases with increasing temperature. Some Al alloys, despite having excellent properties, exhibit low joint efficiency by welding and hence their usage is less favored than other Al alloys that have lower mechanical properties but exhibit better joint efficiency. Some features of Al make it different from steels in terms of weldability. The first feature is the oxide of Al alloy. The special characteristics of Al oxide necessitate some considerations to obtain weldability. The presence of hydrogen is another factor that causes weldability challenges. This is very different from steel in which hydrogen causes completely different problems in welding. Hot cracking is another problem that occurs in the FZ during the final stage of solidification. A similar phenomenon named liquation cracking occurs adjacent to the FZ in partially melted zone (PMZ), which degrades the mechanical properties. The mechanisms of all these phenomena are explained in detail for Al alloys, whose understanding helps to avoid them during welding and improve the weldability.

1.2.1 Aluminum Oxide

The oxide of aluminum (Al_2O_3) is very dense, tough, and thermally stable and has a high melting temperature ($T_m = 2050\,°C$). It is also nonconductive to the electricity. The oxide layer consists of a narrow barrier layer and a thick layer, which have a certain porosity. The presence of alloying elements promotes the formation of complex oxides as well as the change in the thickness of the oxide layer. This oxide layer can trap hydrogen, which changes the characteristics of the oxide layer [19]. The scheme of the oxide layer on the surface of Al in the wet air is shown in Figure 1.5.

The oxide layer can cause an incomplete bonding by inhibiting a metallurgical bonding during welding if it is not removed away by proper methods. In arc welding processes this is done by cleaning effect of the arc in reverse polarity, during which the workpiece is in the positive pole. The oxide layer also influences the plasma spectra and its electronic temperature during arc or laser welding processes [23]. In the absence of the oxide film, the elements are more easily heated to the ionization temperature. Also, the electronic temperature of the plasma is higher, which is due to the absorption of the heat by the oxide film. This causes the depth and the width of the weld to be lower in the presence of the oxide film [23].

Due to its higher melting temperature, the oxide is not melted during welding Al and covers the Al surface with a firm shell, which interferes with the formation of the weld pool [24]. Due to its detrimental effect, the oxide layer has to be removed before welding.

1.2.2 Hydrogen and Pore Formation

Hydrogen is the main gas that forms pores during welding Al alloys. The elements of nitrogen and oxygen do not cause pore formation, as they have a high affinity to make stable nitrides and oxides and therefore are not available in the form of gas. Hydrogen is soluble to a high extent in molten Al, whose solubility decreases abruptly after solidification (Figure 1.6). After solidification, the excess amount of hydrogen, which is not soluble in the solid state, will exit and stay in the melt as pores. This problem is exacerbated when the cooling rate is rapid. By increasing the welding speed, the gas escape is hindered and the pores will become higher in quantity. The position of the welding is also determinant in pore formation. The gas can leave the melt pool easily when welding is performed in the flat position. In the overhead position, there is no escape path for the gas bubbles, and therefore, this position of welding should be avoided for welding Al. One source of hydrogen is humidity, by which the water reacts with Al in the arc space and consequently hydrogen is released according to:

$$2Al + 3H_2O \rightarrow Al_2O_3 + 3H_2 \tag{1.1}$$

The sources of hydrogen are the humidity in the protecting gas, the humidity entered from the atmosphere, and the residues on the surface of the workpiece or the filler, such as paint, oil, and hydroxides.

Another source of hydrogen is the oxide layer of the Al. The pores that result from the oxide layer of the base material appear as uniform coarse pores over the weld length. The pores that result from the hydrogen of the oxide layer of the filler material appear as uniform fine pores [19]. The thicker the oxide layer, the higher the amount of hydrogen. The thickness of the oxide layer, as mentioned before, depends on the alloying elements or, in other words, the type of Al alloy. For example, AA2198 possesses a thinner oxide layer than AA2196. Another factor that determines the amount of hydrogen from the oxide layer is the thickness of the Al

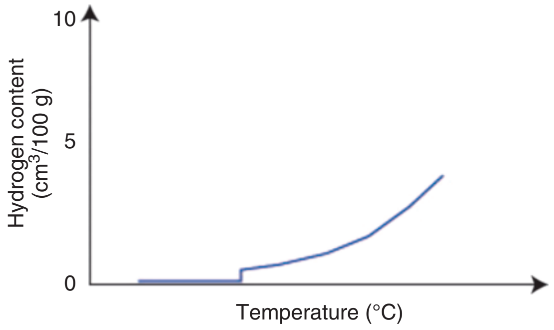

Figure 1.6 Solubility of hydrogen in aluminum at various temperatures.

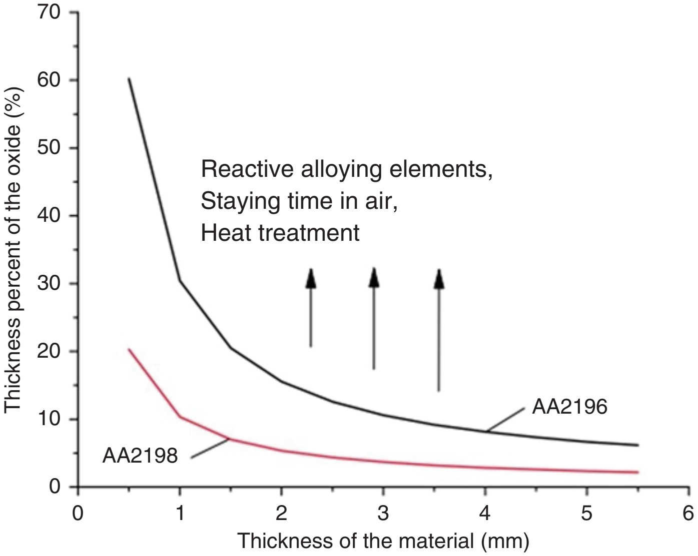

Figure 1.7 Relation between the portion of the oxide layer and the thickness of the sheet for two Al alloys. Source: Adapted from [19].

sheet [19]. By increasing the thickness of the Al sheet, the ratio of the oxide/total mass of Al decreases, which in return lowers the amount of hydrogen introduced. The portion of the oxide layer decreases exponentially with thickness, as shown schematically in Figure 1.7. The annealing temperature and time can also increase the thickness of the oxide layer.

The oxide layer can also produce pores in another way. During laser welding of Al, the high temperature inside the keyhole vaporizes the oxide layer at the interface, which appears as pores (red squares in Figure 1.8) [25]. These pores are distinguished by the pores caused by the keyhole instability, which form at the bottom of the weld (blue squares in Figure 1.8). The mechanism of pore formation by keyhole is explained in detail in Chapter 3. Also, the mechanism that controls these kinds of pores will be discussed. As an example, introducing a gap between

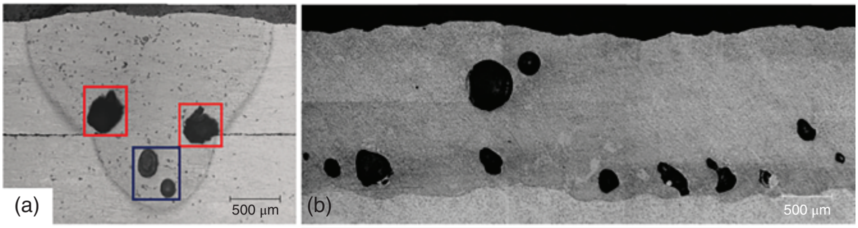

Figure 1.8 Pores caused by oxide layer (inside the red squares) during laser welding of a 6061 alloy. (a) Cross section view and (b) longitudinal view. Source: Ref. [25]/with permission of Elsevier.

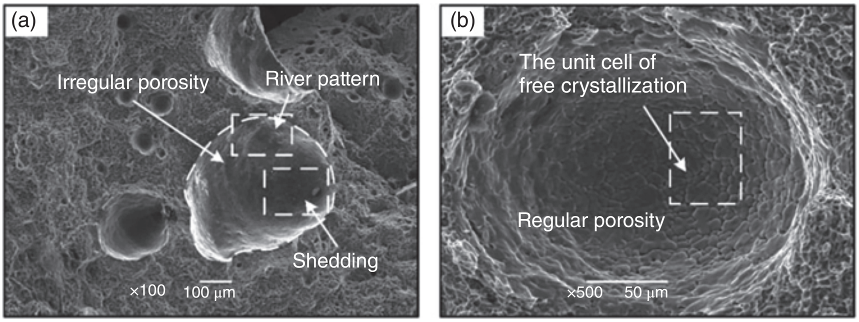

Figure 1.9 SEM image of (a) technical or keyhole-induced pore and (b) metallurgical pore. Source: Ref. [27]/Taylor & Francis.

the plates provides a vent to relieve the pressure, causing a more stable keyhole [25]. This leads to less pore formation and a stronger weld.

Based on these, the surface of Al needs to be cleaned before welding either by mechanical or chemical methods [19]. The degree of removal of the surface oxide depends on the thickness of the oxide layer. Considering that the thickness of the oxide is not uniform (see Figure 1.5), the removal of the surface should make sure that the oxide layer is removed completely. The mechanical methods of removing the oxide layer, especially the milling processes, are the most proper ones. Though in these methods the surface becomes wavy, it is free of adhered deposits, which appear after chemical methods [2]. One example of the chemical cleaning method is soaking in 20% sodium hydroxide solution and subsequent soaking in dilute nitric acid to neutralize the residual alkali before welding [26]. Due to the rapid formation of the oxide layer, even in the vacuum, the welding process should be carried out right after the surface treatment.

In fusion welding processes wherein a keyhole exists, such as laser beam welding, another kind of pores can form during welding. The source of these pores is not hydrogen, but the metallic vapor and the shielding gas entrapped by the keyhole collapse. When the melt pool solidifies rapidly, these entrapped vapors and gases do not have enough time to escape from the melt pool, forming a keyhole-induced pore [26]. A scanning electron microscopy (SEM) image of this hole is provided in Figure 1.9a. These pores have irregular shapes with step-like inner walls and traces of solidification contraction [26]. The pores that are caused by hydrogen or by metal vapor produced by the burning of the metal elements are referred to as metallurgical pores [27]. The metallurgical pores have regular shapes, and the inner interface is smooth due to free crystallization cell boundary on the wall of the pore. The internal pressure of accumulated hydrogen inside the pore in the solidification stage initiates after nucleation of the pore and then the continuous diffusion of hydrogen into it [27]. The pores formed by keyhole collapse in the unstable welding pool are also referred to as the technical pores, which are irregular and large [27]. These pores can be reduced by controlling the process parameters. The pores caused by hydrogen are smaller in size than the ones induced by instability of the keyhole [28]. The details of the formation of the technical pores are addressed in Chapter 3.

1.2.2.1 Effects of Porosity on the Mechanical Behavior

The porosity in the weld metal of Al reduces the ductility, tensile strength, and fatigue stress [29]. Deformation concentrates around the porosities, and a higher strain rate exists in the regions with these defects, which subsequently reduces the ductility [30]. If the porosity percent is lower than 4% volume, it does not influence the static mechanical behavior [31]. The pores exhibit on the fracture surface, showing their contribution to the initiation of the fracture [32].

The fatigue strength will not be influenced if the diameter of the pores is less than 0.2 mm, as these pores are present in globular form. By increasing the diameter of the pores, the dynamic behavior will be influenced. The dispersion of the pores is also important in the determination of the mechanical behavior. A solitary scattered pore or pore nest is less detrimental than line pores with very small sizes. In the welded specimens without any pores, the fatigue crack initiates at the surface. While in the presence of porosity, the fatigue cracks initiate near the edge of the porosities, and by increasing the porosity, the fatigue stress reduces [29, 33].

The pores are not the only cause of degradation of the mechanical properties. The cracks made by metallurgical phenomena such as hot cracking that occurs during solidification also have an impact. The existence of various defects such as pores and cracks in the FZ is reported in the literature [34]. Understanding the mechanism of formation of these cracks is necessary to avoid them during welding.

1.2.3 Hot Cracking

SC is a very typical failure in Al alloys. In contrast to pure metal, alloys solidify within a temperature range where both solid and liquid phases are present. A simple explanation of this crack is provided in Figure 1.10. The occurrence of SC is accompanied by local stress or strain as well as eutectic compounds with low melting temperatures present in the grain boundaries between the growing dendrites. Usually, Al alloys are more susceptible to this cracking than pure Al [35]. At the final stage of the solidification process, while the grains are solidified the eutectic phase is present in the form of liquid between the grains. The shrinkage of solidification causes the just solidified grains to move with respect to each other whose boundaries are filled with this liquid. This causes a separation of the grains, which, by further cooling and shrinkage, leads to the formation of cracks lined up together (Figure 1.10a). When enough liquid as well as a path for this liquid to fill these cracks are available, a healing process occurs that eliminates SC, as shown in Figure 1.10b.

Various theories have been proposed to address the details of hot cracking. During solidification when cooling down the melt, there is a slurry stage where both solid and liquid phases are present and the dendrite arms of the solid phase are not coalescent. The temperature is between the temperature of coherency and the liquidus ($T_{coh} < T < T_l$). By further cooling, when the temperature is below the coherency temperature and above the solidus temperature, the dendrites become coalescent and form a coherent solid network named mushy zone ($T_s < T < T_{coh}$) [36]. The schematics of these regions (slurry and mushy zones) are shown in Figure 1.11.

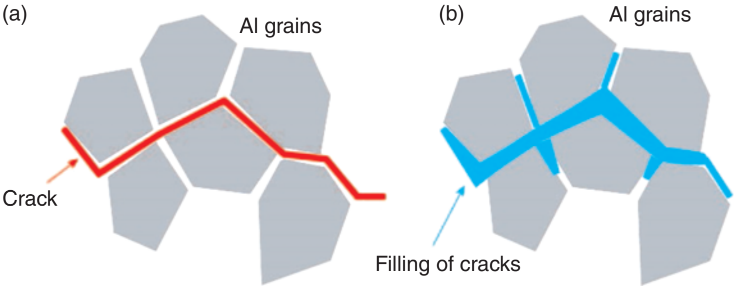

Figure 1.10 (a) The contribution of eutectic compounds at the grain boundaries to the formation of solidification cracking. (b) Filling of the crack by available eutectic compound.

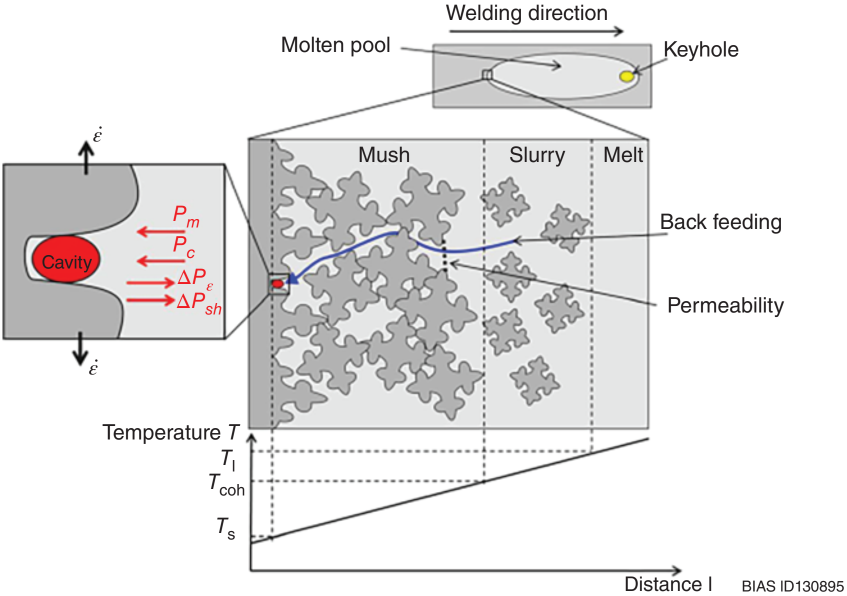

Figure 1.11 Schematic diagram of the semisolid molten pool. Source: Ref. [37]/Springer Nature.

According to “shrinkage-brittleness theory,” when the dendrites grow during cooling, they form a network of solid structures below the coherence temperature, which is above the solidus temperature. By further decreasing the temperature below the coherence temperature, a high strain rate develops in the solid structure, which may cause the dendrite arms to open and get separated in the coherent zone. The remaining liquid may not penetrate the bridges between the solids due to low permeability of the solid and high viscosity of the liquid. This process continues until the solidus temperature is reached. The interval between the coherence temperature and the solidus temperature is named the effective interval, which is referred to as the brittle temperature range (BTR). At the starting point of BTR, the dendrites start to connect and hence the thermal stresses form. At the end

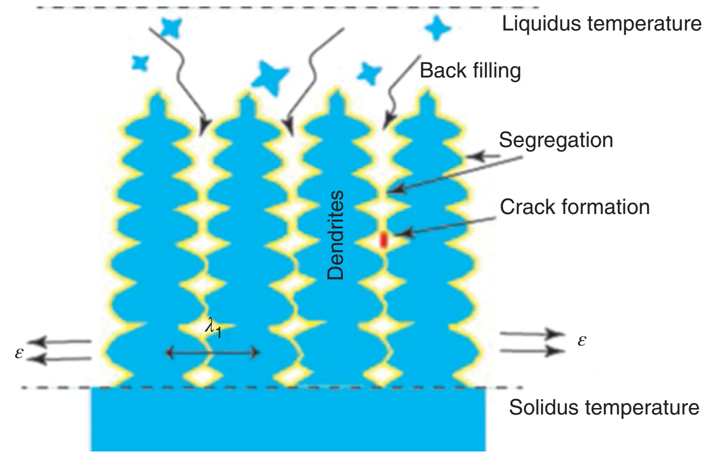

Figure 1.12 Schematic model of hot cracking and its influencing variables.

of BTR, the dendrites are coalescent and hence this region gains a strength [38]. When the shrinkage strain increases over a critical point in BTR, this region cannot bear the resultant load and thus solidification crack appears [39]. This can be schematically explained as shown in Figure 1.12. SC occurs in the solidification interval (ψ) in the temperature range of liquid and solid (T_L and T_S) wherein cavities in the inter-dendritic space form due to the solidification shrinkage and thermal contraction. These cavities cannot be filled with the remaining melt. The following factors influence the refill process of the inter-dendritic space [40]:

- The length of solidification, ψ: This is the distance which the remaining melt should travel to fill the cavity.
- Solidification time of the weld pool: It is the available time span for the remaining melt to flow to the cavities.
- Permeability of the melt in the solidification interval: It shows how easily the remaining melt flows between the dendrites. After a certain distance, the inter-dendritic space becomes too small to allow for the remaining melt to flow in. This can be metallographically quantified as the primary dendritic or cell-arms distance (λ_1). The permeability of a dendritic network (k_{dend}) is obtained from [41]:

$$k_{dend} = \frac{f_l^3 \lambda_2^2}{180 f_s^2} \tag{1.2}$$

  where λ_2, f_s, and f_l are the secondary dendrite arm spacing, the fraction of solid, and the fraction of liquid, respectively.
- Segregation in the inter-dendritic network: Through this, the remaining melt is enriched with low-melting eutectics with a wide solidification range.
- The strain and strain rate, which act on the thin liquid film between the dendrites and cause the dendrites to open cracks.
- The tensile stresses, which develop in the coalescent part of the two-phase region (solid–liquid) where the refill of the remaining melt cannot occur.

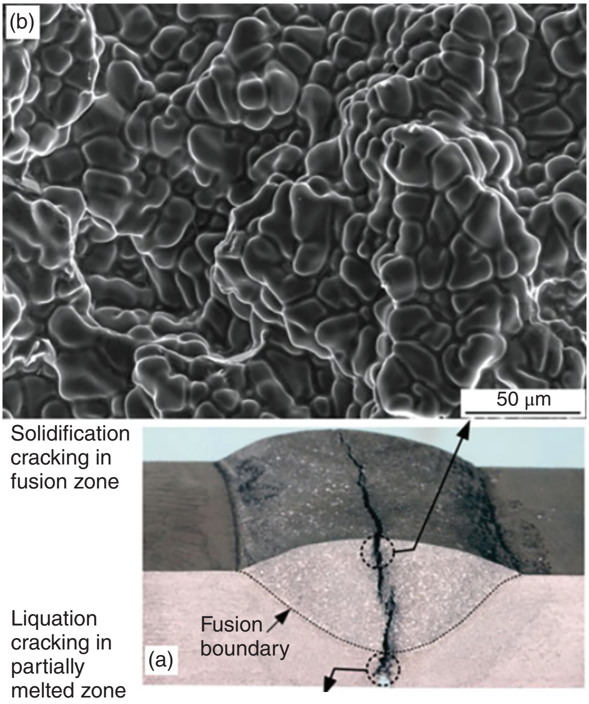

Figure 1.13 Fracture surface of an SC developed during welding of an AA6061. (a) Macro image of the weld. (b) SEM image of the crack surface. Source: Ref. [43]/Springer Nature.

SC can be distinguished in several ways. Usually, it occurs at the center of the weld pool before the weld is cooled down. When a weld with an SC is loaded to failure, the fracture surface analysis by SEM can reveal some unique characteristics of the SC. The main feature of SC is a free solidified fracture surface on which low melting eutectic is present (Figure 1.13) [42]. Along with SC, another form of hot cracking, called liquation cracking, may occur, which is explained at the end of this section.

The commercial pure Al is not susceptible to SC due to the absence of the solidification temperature range [35]. The composition of the melt zone is the main parameter that determines the occurrence of SC. The binary systems of Al alloys such as Al—Si, Al—Cu, and Al—Mg are susceptible to hot cracking in specific ranges of composition. SC is more likely to occur in multi-element Al alloys, for example precipitation-hardened alloys, as the number of compounds that promote hot cracking increases. In fact, the alloying elements promote the segregation during dendrite growth, which appear as low-melting compounds between the dendrites. SC, as a metallurgical defect, occurs during cooling in the range of liquidus–solidus temperature range under residual stress in the weld zone and in the weld crater in the presence of the alloying elements. The larger the solidification interval and the higher the residual stress, the more probable the occurrence of SC. The effect of the solidification interval on the hot crack tendency is schematically shown in Figure 1.14. This kind of diagram gives some important criteria that can be used to assess the SC sensitivity. The dwelling time in the interval and the span of the concentration ($\Delta C = C_{\max} - C_1$) are two features that yield good measures of the segregation and

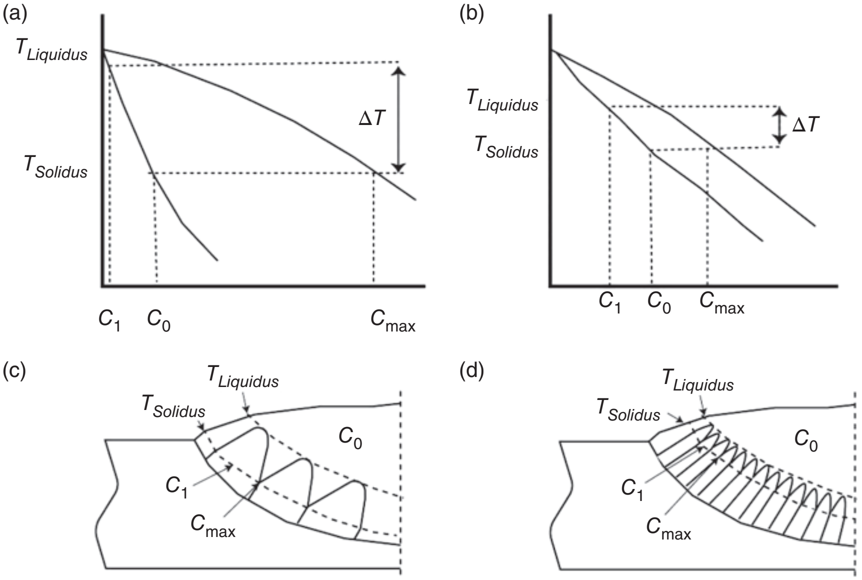

Figure 1.14 Effect of (a and b) solidification interval (ΔT) on (c and d) the segregation of elements at the center of the weld.

consequent SC. When ΔT is large (Figure 1.14a, c), the segregation is pronounced, and when ΔT is small (Figure 1.14b, d), the segregation is low. The liquidus and solidus temperatures can be calculated by the silicon equivalent concept, whereby the chemical composition of a multi-element weld was simplified using an Al/Si binary system. In this way, the silicon equivalent of each element ($Si_{eq}^{X_i}$) is obtained by its corresponding equation, and subsequently, the total Si equivalent of the melt (Si_{eq}) can be obtained by the following relationship [37]:

$$Si_{eq} = [Si] + \sum Si_{eq}^{X_i} \tag{1.3}$$

The liquidus and solidus temperatures and hence ΔT can be easily obtained by knowing this Si_{eq}.

When Al is alloyed above the maximum solubility, eutectic microstructure forms, which reduces the hot crack susceptibility. The results of the evaluation of the hot crack susceptibility of an AA6xxx alloy (Al—Mg—Si system) by ring casting samples [44] are shown in Figure 1.15. The increase in the alloying elements reduces the crack length and thus the SC susceptibility. The chemical composition and the resulting solidification range cannot always be solely used as a criterion for prediction of SC. The situation was reported in which some solidification cracks were present locally, despite being in the safe composition range. This indicates that other factors are needed to be taken into account. The induced strain rate during solidification plays an important role in SC occurrence [45]. The strain rate is dependent on the thermal gradient and cooling rate as well as the speed of backfilling the cracks. A two-level hot crack index was proposed by which both the composition and the thermal effects of the process are considered [46]. The shrinkage during solidification and thermal contraction on the one hand develop stress that promotes SC. On the other hand, they induce a pressure drop between the solidified dendrites, which causes the liquid to flow against the solidification direction. This makes a backfilling whose cause is a pressure difference [36]. This pressure drop (Δp_c), also called cavitation depression, which is caused by shrinkage (Δp_{sh}) and deformation (Δp_{def}), is obtained through [46]:

$$\Delta p_c = \Delta p_{sh} + \Delta p_{def} = \frac{180}{\lambda_2^2}\frac{\upsilon_T \beta \mu}{G}A + \frac{180}{\lambda_2^2}\frac{(1+\beta)\mu\dot{\varepsilon}(T)}{G^2}B \tag{1.4}$$

where λ_2, υ_T, β, μ, G, and $\dot{\varepsilon}(T)$ are the secondary dendrite arm spacing, the velocity of isotherms, the shrinkage factor, the liquid viscosity, the thermal gradient, and the strain rate of deformation, respectively. A and B are obtained from [46]:

$$A = \int_{T_s}^{T_l} \frac{f_s(T)^2}{(1-f_s(T))^2}\,dT$$

$$B = \int_{T_s}^{T_l} \frac{f_s(T)^2 \int_{T_s}^{T_1} f_s(T)dT}{(1-f_s(T))^3}\,dT \tag{1.5}$$

where $f_s(T)$, T_l, and T_s are the fraction of solid at temperature T, the liquidus temperature, and the coherency temperature, respectively. The larger the parameters A and B, the larger the pressure drop and the higher the tendency for hot cracking [46]. Parameter A depends on the solidification temperature range and can be used as a criterion to predict the hot cracking susceptibility based on the chemical composition. The Rappaz Drezet Gremaud (RDG) theory is based on the critical depression criterion, above which the strain rate is high enough to induce cracking in the coherent zone [47]. The hot cracking susceptibility depends on the maximum strain rate that can be endured in the mushy zone and is obtained from:

$$\dot{\varepsilon}_{p,\max} = \frac{\lambda_2^2}{180}\frac{G}{(1+\beta)\mu}\Delta p_c - v_T\frac{\beta}{1+\beta}A \tag{1.6}$$

The higher $\dot{\varepsilon}_{p,\max}$, the lower the hot cracking sensitivity, as the higher strain rate reduces the critical strain at which the crack initiates [48]. This equation considers the effect of both the chemical composition (through parameter A) and the thermal effects of the process (through parameters (G, λ_2) [46]. Positive strain rate refers to a tensile load, and negative strain rate refers to a compressive load. When the critical strain rate is negative, it means that the strain developed during solidification should be compressive to avoid SC. Usually, as the stresses developed during solidification are tensile, the strain rate would also be tensile, meaning that the strain rate cannot be smaller than the critical strain rate and therefore the risk of SC is very high [49]. By choosing a proper filler material and dilution, the critical strain rate can be improved to avoid SC. An example is welding of AA606 with AA4043 filler material by which the critical strain rate was increased from −0.16%/s at 0% dilution to 0.35%/s at 16% dilution of AA4043 filler material [50]. The role of Si in this case is to refine the grains and change the bead shape, which both improve the SC.

There are factors other than the chemical composition and the welding parameters that affect the SC behavior. Figure 1.16 shows how the weld seam shape in

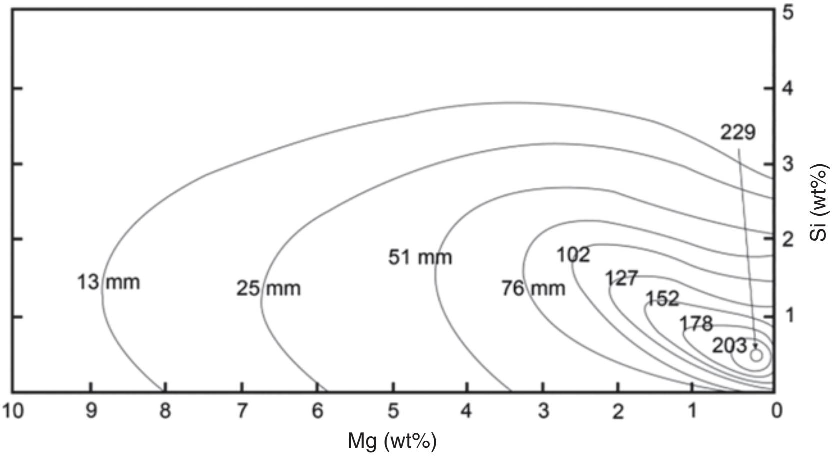

Figure 1.15 Length of the solidification crack with respect to the amount of Si and Mg for AA6xxx. Source: Ref. [40]/with permission of Dr. Martin Bielenin.

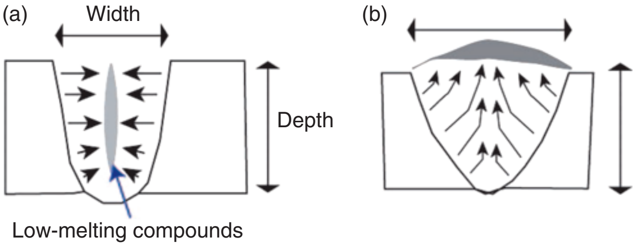

Figure 1.16 Effect of weld pool shape on the segregation and solidification cracking in a single-pass weld with (a) a high depth-to-width ratio and (b) a low depth-to-width ratio.

a single-pass weld affects the solidification and promotes SC. In fact, the shape and the size of the weld zone cause the low-melting compounds to segregate in the solidification front whose edges are parallel on both sides. Deep weld pools are prone to this type of SC. For example, in laser welding by which a narrow weld zone is created and the distance from the weld center line to the fusion line is small, there is a high susceptibility to SC due to this pronounced segregation [51]. The effect of depth-to-width ratio on the segregation and SC is shown in Figure 1.16.

Welding speed and heat input affect the shape of the weld pool and hence the SC. When the welding speed is low, the weld pool solidifies in a curvature toward the weld line, pushing the low-melt compounds to the weld pool. When the welding speed is high, the solidification fronts grow parallel and the low-melt compounds segregate at the center of the weld promoting SC (Figure 1.17).

Therefore, the following parameters can be controlled to lower the tendency of SC [2]:

- The increase in the number of passes and consequent decrease in the size of each pass decrease the SC susceptibility.

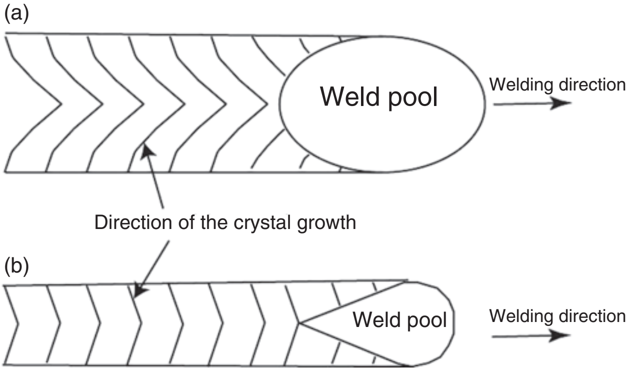

Figure 1.17 Effect of the welding speed on the solidification cracking at (a) low welding speed and (b) high welding speed.

- The low-melting compounds are formed from impurities, which usually are introduced from the base material. So, lowering the dilution decreases the percentage of impurities in the FZ and lowers the tendency for SC. The low dilution can be obtained by proper selection of welding process, proper selection of the welding parameters, and the weld seam preparation. For example, V-grooves result in lower dilution than square edges.
- Lower welding speed causes the solidification fronts to be curved at the center, leading to pushing off the impurities into the weld pool and weld surface as slag. Hence, the tendency for SC decreases.

Another effective method to alleviate the solidification crack is to control the grain size and morphology. Small grain size causes a high capillary pressure (p_c) of the liquid, whose value is obtained from [37]:

$$p_c = \frac{4\gamma}{h} \tag{1.7}$$

where γ and h are the surface tension and the thickness of the liquid between the equiaxed grains, respectively. Grain refinement causes the thickness of the liquid film on the grain boundaries to decrease, which subsequently increases the capillary pressure, which inhibits the hot crack propagation. The equiaxed grains are present at the centerline of the weld to reduce SC in contrast to the columnar grains [52]. This is because lower strain is concentrated in the equiaxed grains. Furthermore, in the fine equiaxed grains, higher grain boundaries exist, which permits the liquid to have a higher permeability through the grain boundary, causing higher deformation to be tolerated [52]. These two factors, the width of the equiaxed zone in the middle of weld (w_{eqx}) and the grain size of this region (d_{eqx}), are unified in a parameter named the width-specific number of grain boundaries (N_{GB}), which is obtained from [53]:

$$N_{GB} = \frac{w_{eqx}}{d_{eqx}} + 1 \tag{1.8}$$

Grain refinement in the welding zone can be obtained by addition of Ti, which promotes the nucleation and increases the width of equiaxed zone at the center by

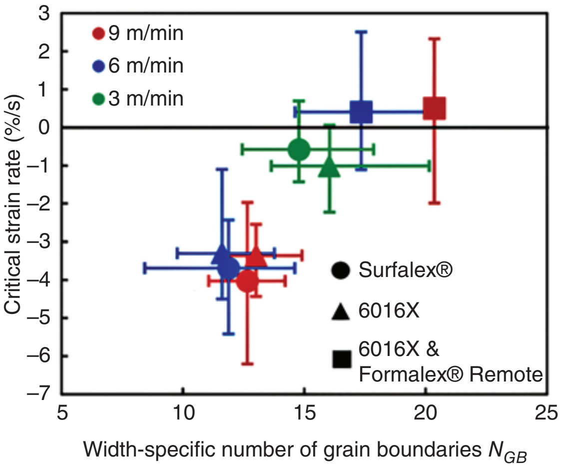

Figure 1.18 Dependency of critical strain rates of the weld with the width-specific number. Source: Ref. [53]/Sage Publications/CC BY 4.0.

restricting the growth during solidification, causing a transition from columnar to equiaxed growth [53]. Addition of Ti is more effective than controlling the welding parameters to change w_{eqx} and the grain size [53]. Figure 1.18 shows how the critical strain rate is increased when N_{GB} increases with the addition of Ti into the weld metal.

However, lowering the grain size below a critical size increases the susceptibility to hot cracking due to decreased permeability [54]. Thus, an optimum grain size exists that helps to mitigate SC. Figure 1.19 schematically presents how the grain size affects the SC sensitivity.

A criterion to figure out whether a composition of Al is not susceptible to cracking is when the following quantity is lower than a critical value [55]:

$$\left|\frac{dT}{d(\sqrt{f_S})}\right|_{\text{at }(\sqrt{f_{SS}}=0.95)} \tag{1.9}$$

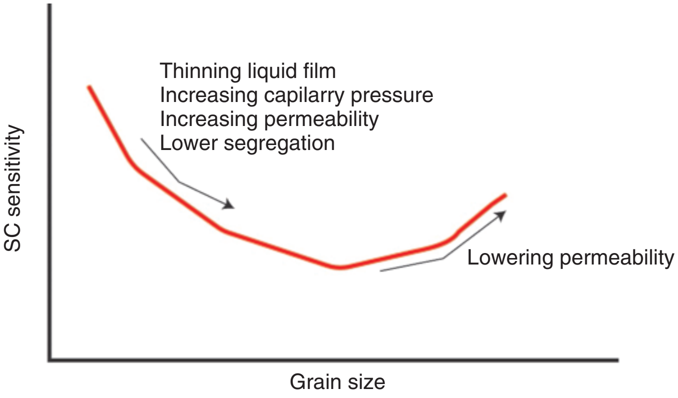

Figure 1.19 Schematic curve of the effect of grain size on SC sensitivity.

where T is the temperature, f_S is the solid fraction, and f_{SS} is the solid fraction at which the inter-dendritic separation occurs (about 0.9). The critical value is calculated from [55]:

$$\left|\frac{dT}{d(\sqrt{f_S})}\right| = \frac{2(1-k)(T_m - T_E)\sqrt{f_S}}{1-f_S} \tag{1.10}$$

where k is the equilibrium segregation coefficient, T_E is the eutectic temperature, and T_m is the melting temperature. $\frac{dT}{d(\sqrt{f_S})}$ can be obtained using commercial thermodynamic software by plotting the temperature as a function of the solid fraction. In this way, it is possible to predict whether a composition is susceptible to SC or not. A high value of this index near $\sqrt{f_S} = 1$ indicates that the neighboring dendrites are not bridged well to resist cracking by slowing the lateral growth rate of the grains, where R is the characteristic value of the grain (Figure 1.20) [56].

An example is presented for Al—Si alloy, whose binary phase diagram is shown in Figure 1.21a. According to this figure, the following values are obtained:

$$(1-k)(T_m - T_E) = \Delta T_{\max} = 75 \tag{1.11}$$

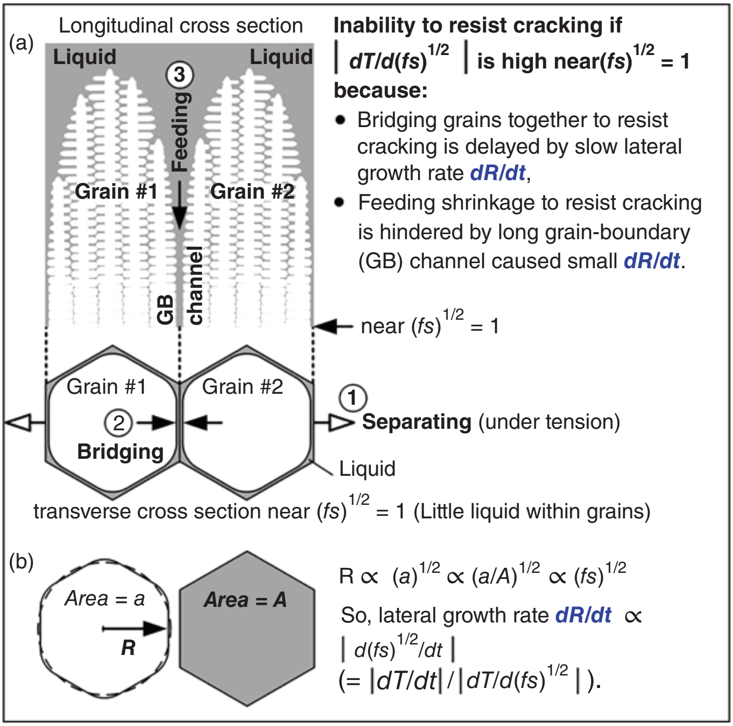

Figure 1.20 Dependency of the lateral growth of the grains with the SC susceptibility index. Higher index means the lateral growth is lower than the axial growth, making the backflow difficult to overcome the crack. (a) Bridging mechanism. (b) Characteristic value of the grain. Source: Ref. [56]/with permission of Elsevier.

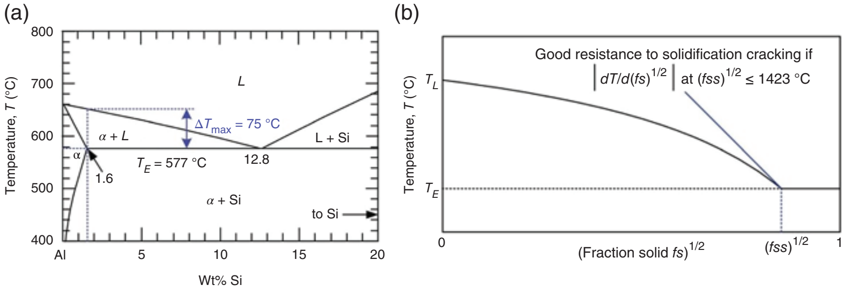

Figure 1.21 (a) Al/Si binary phase diagram. (b) Plot used to predict the SC by knowing the critical value. Source: Ref. [55]/Sage Publications.

$$k = \frac{1.6}{12.8} = 0.125 \tag{1.12}$$

Therefore:

$$\left| \frac{dT}{d(\sqrt{f_S})} \right| = \frac{2\Delta T_{\max}\sqrt{f_S}}{1 - f_S} = \frac{150\sqrt{0.9}}{1 - 0.9} = 1423^{\circ}\mathrm{C} \tag{1.13}$$

The quantity $\left| \frac{dT}{d(\sqrt{f_S})} \right|$ is used as SC susceptibility index. The plot of temperature versus the square root of the solid fraction is shown in Figure 1.21b. This plot changes when using various filler materials and various dilutions. This plot helps to predict the SC sensitivity by using the above equation.

The choice of filler material is based on the flow behavior of the melt, the mechanical strength of the weld, and the hot cracking tendency of the base material [19]. This equation helps to select a filler material for a susceptible Al alloy to overcome the SC during welding by knowing the dilution. The limitation of this approach is that it is based on binary phase diagram, meaning that it neglects other alloying elements not present in the binary phase diagram. For ternary systems, similar curves like Figure 1.21b can be obtained for various amounts of one element while the other element is held constant [57]. It also does not take into account the diffusion in the solid state by which the alloying elements at the solidification front may deviate from the equilibrium state far from the phase diagram. The back diffusion from the inter-dendritic liquid to the solid dendrites decreases the SC susceptibility [57]. By considering the back diffusion, the solid fraction is modified, and consequently, the SC susceptibility index is modified according to the following equation [58]:

$$\left| \frac{dT}{d(\sqrt{f_S})} \right| = \frac{2(1-k)(T_m - T)\sqrt{f_S}}{1-(1-2\alpha' k)f_S} = \frac{2(1-k)(-m_L)C_o\sqrt{f_S}}{1-(1-2\alpha' k)f_S}[1-(1-2\alpha' k)f_S]^{\frac{k-1}{1-2\alpha' k}} \tag{1.14}$$

where α' is obtained from:

$$\alpha' = \alpha\left[1 - \exp\left(-\frac{1}{\alpha}\right)\right] - \frac{1}{2}\exp\left(-\frac{1}{2\alpha}\right) \tag{1.15}$$

$$\alpha = \frac{4D_s t_f}{\lambda_2^2} \tag{1.16}$$

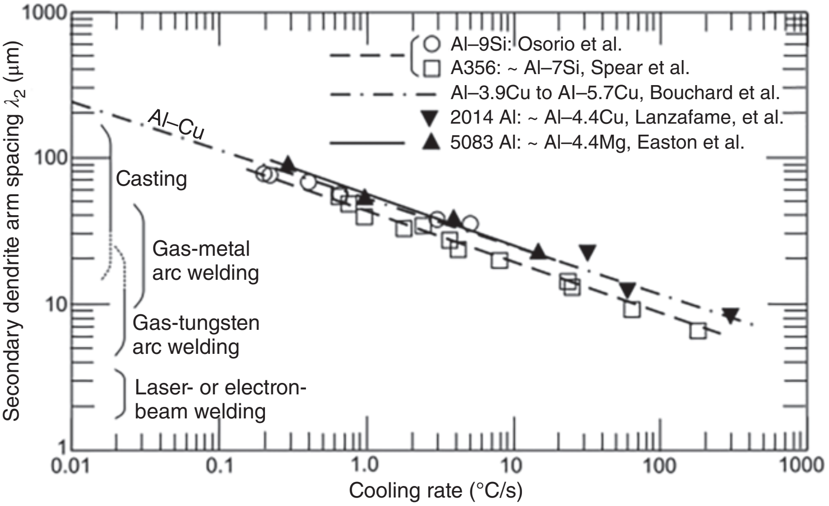

Figure 1.22 Secondary dendrite arm spacing of some Al alloys as a function of cooling rate. Source: Ref. [58]/with permission of Elsevier.

D_s is the diffusion coefficient of solute in solid and t_f is the local solidification time. In the extreme case where $\alpha' = \alpha = 0$, the simple criterion based on the Scheil equation is obtained where no back diffusion occurs $\left(\left|\frac{dT}{d(\sqrt{f_S})}\right| = \frac{2(1-k)(T_m-T_E)\sqrt{f_S}}{1-f_S} \text{ Eq. (1.10)}\right)$. The Scheil equation assumes that there is an equilibrium at the interface of liquid and solid, there is a complete diffusion in liquid, and there is no diffusion in solid. In another extreme case where $\alpha = \infty$, a complete solid-state diffusion occurs and lever-arm rule for an equilibrium state solidification is held. The secondary dendrite arm spacing λ_2 is a determinant factor, which itself is dependent on the cooling rate. The higher the cooling rate, the lower the secondary arm spacing. The range of this quantity is shown for various welding processes as well as casting in Figure 1.22. The back diffusion can more effectively reduce the SC when the cooling rate is low. The reason that back diffusion reduces the SC is the consumption of the alloying element in the liquid inside the inter-dendritic space [56].

Another modification to the SC susceptibility index based on the Scheil equation is developed for various solidification rates. The basis of this approach is to consider the effect of solidification rate on the T–f_S curve [59]. The downward shift of this curve results from the decrease in the eutectic temperature due to fast solidification rate (Figure 1.23a). The new SC susceptibility indexes derived from the new T–f_S curves for various processes with their specific solidification rates, are shown in Figure 1.23b. The maximum index increases with an increasing solidification rate. Also, the composition at which the maximum sensitivity occurs increases. Using the previous approach based on back diffusion, the laser welding with smaller α' value results in a smaller composition at which the maximum susceptibility exists, which does not align with the experiments.

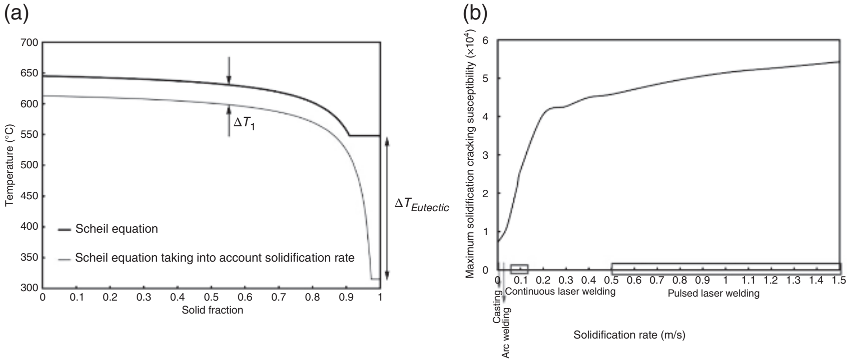

Figure 1.23 (a and b) $T-f_S$ curves based on the Scheil equation taking into account the solidification rate. Source: Ref. [59]/Springer Nature.

This approach is used to compare the weldability of a composition system at various solidification rates. To compare various composition systems (Al binary systems such as Al—Cu, Al—Mg, and Al—Zn), the back diffusion at eutectic temperature through the parameter αk is included in the SC susceptibility index. In this approach, the maximum value of $\left|\frac{dT}{d(\sqrt{f_S})}\right|$ is considered as an index for SC susceptibility. This approach justifies well why Al—Mg alloys, despite having a wide solidification temperature range, show a lower crack susceptibility due to their high value of k at eutectic temperature [56]. Figure 1.24a and b show the temperature versus the square root of the solid fraction when $\alpha = 0.05$ for Al—Cu and Al—Mg alloys, respectively. The corresponding crack susceptibility indexes versus the alloy content for various values of α are shown in Figure 1.24b and c. A significant decrease in the maximum index is observed for Al—Mg alloy at high values of α, which is due to the high value of k.

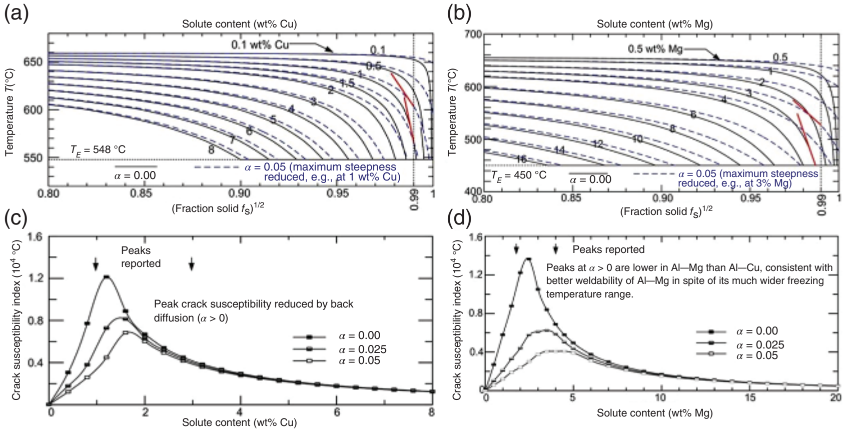

Figure 1.24 Temperature versus the square root of the solid fraction for (a) Al—Cu and (b) Al—Mg alloys. The corresponding crack susceptibility indexes versus the alloy content for various values of α for (c) Al—Cu and (d) Al—Mg alloys. Source: Ref. [56]/with permission of Elsevier.

In some processes like laser beam welding, the vaporization leads to a change of alloying elements [60], which is not considered in the equations of SC susceptibility index. For instance, the burning of Mg element during laser beam welding of 6xxx alloys leads to a decrease in the strength of the weld, and hence, 5xxx filler wires are used to compensate for the Mg content [61]. This needs to be taken into account when using these indexes.

A variant of hot cracking that locally occurs close to the FZ in the PMZ is liquation cracking, which is caused by melting the constituents of low melting temperatures such as eutectics or inclusions. This type of crack is also more likely for precipitation-hardened alloys, especially when there is no time during heating to dissolve these precipitates. The liquation occurs close to the FZ in the grain boundaries. Due to a large extent of the semisolid region and high thermal conductivity of Al, the region of PMZ is relatively large during welding Al alloys. A simple criterion to predict the occurrence of liquation cracking in PMZ is explained by the solid fraction in both PMZ and FZ adjacent to the PMZ [43]. The contraction stress imposed by the FZ on the PMZ can cause liquation cracking when the solid fraction in FZ is higher than the one in the PMZ, as shown in Figure 1.25b. In this state, the strength of the PMZ is not enough to resist the contraction caused by solidification in the FZ. When the solid fraction in PMZ is higher than in FZ, it can resist the contraction and no liquation cracking occurs (Figure 1.25b). Seemingly, the supply of the liquid from the FZ to the cracks in PMZ heals the crack in this region and prevents the liquation cracking. The occurrence of liquation cracking also depends on the microstructure and the temper of the base material. For instance, AA6061-T6 is more susceptible to liquation cracking than AA6061-T4, as the former has a coarser grain size with larger amounts of Si-rich eutectic compounds at the grain boundaries [62].

The composition of the Al alloy determines the thermal conductivity and hence the solidification rate [35]. This in turn determines the strain rate and hence the susceptibility to SC. So, the effect of chemical composition on SC is multifactorial, whose effect can be understood in more detail by simulation.

1.3 Thermal Cycle and Its Effect on the Weld Zone

Precipitation hardening alloys of Al undergo a thermal cycle in the HAZ, which can cause over-aging through which semi-coherent θ' phase converts to more stable θ. This causes a softening in the HAZ of the welds, which deteriorates the integrity of the structure. The microhardness test is a useful method to measure the mechanical properties in various regions of the welds by giving a hardness profile resolving different regions. A schematic of the microhardness distribution in HAZ with respect to the distance from the FZ boundary is shown in Figure 1.26. Adjacent to the FZ boundary, the hardness is lowest due to the solution heat treatment caused by the heat of the welding process (zone 1). In zone 3, the precipitates change to more stable θ and the percentage of this change increases with an increase in the pick temperature as it approaches the FZ boundary. Right adjacent to the FZ boundary, also named partially melted zone, the hardness can be recovered partially

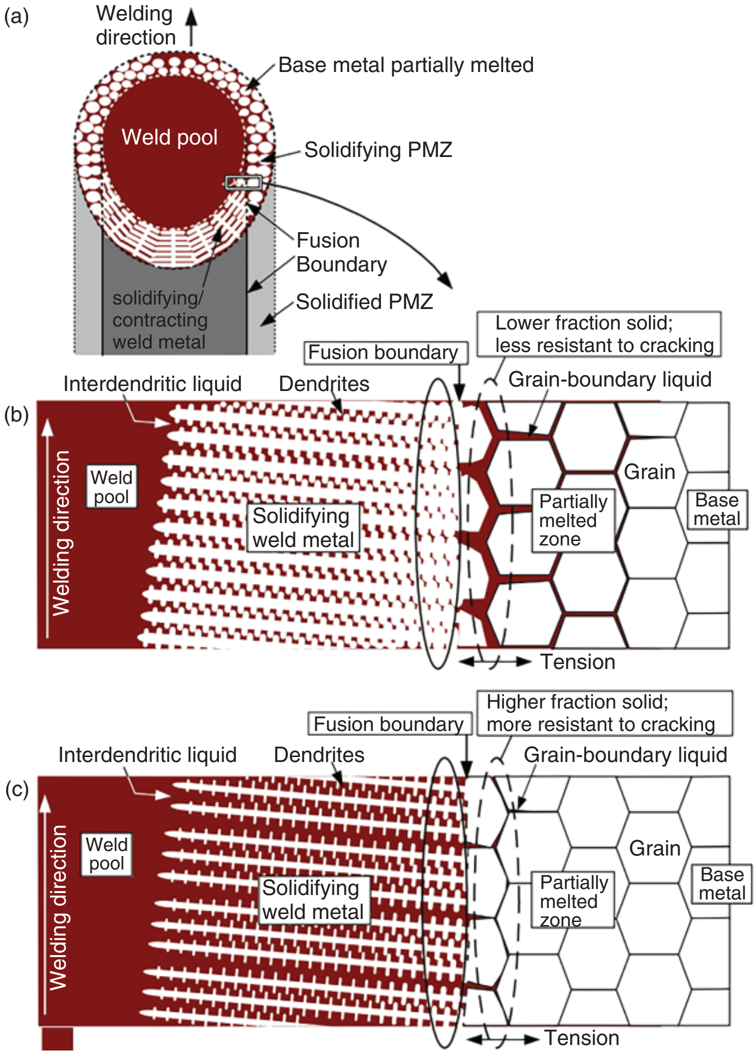

Figure 1.25 (a) Top view of the weld metal. (b) PMZ susceptible to liquation cracking. (c) PMZ resistant to liquation cracking. Source: Ref. [43]/Springer Nature.

by natural aging after welding (region *B* in Figure 1.26) [63]. Through an artificial aging after welding, the hardness of this region can be recovered completely (region *A* in Figure 1.26). Farther from this region toward the base material is a region that is partially solutioned and mainly in the over-aged state. Through artificial aging, the hardness can be partially recovered leaving this region to have the lowest hardness (region 2 in Figure 1.26).

To fully recover the original hardness, a PWHT consisting of a solutioning heat treatment and subsequent aging is needed [64]. In this way, the stable phases formed in the over-aged regions dissolve during solutioning and change to fine and uniformly dispersed semi-coherent precipitates during aging.

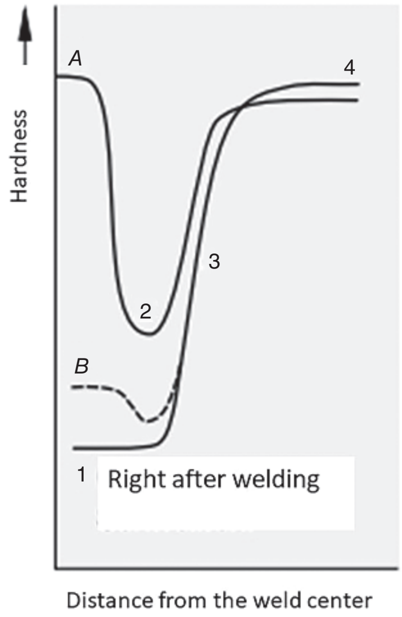

Figure 1.26 Schematic of hardness distribution in the HAZ of welded age-hardened aluminum alloy (curve 1). Source: Ref. [2]/Springer Nature.

Figure 1.27 shows a schematic of decrease in hardness in the weld zone and HAZ of a HTA welded by the gas metal arc welding (GMAW) process. The microstructure and the consequent mechanical properties (hardness) are recovered through solutioning and aging, as can be observed in Figure 1.27.

One strategy to overcome the softening in the HAZ is using the welding processes with a low heat input, such as laser welding, friction stir welding (FSW), and cold metal transfer (CMT) [65]. These processes are discussed in the following chapters.

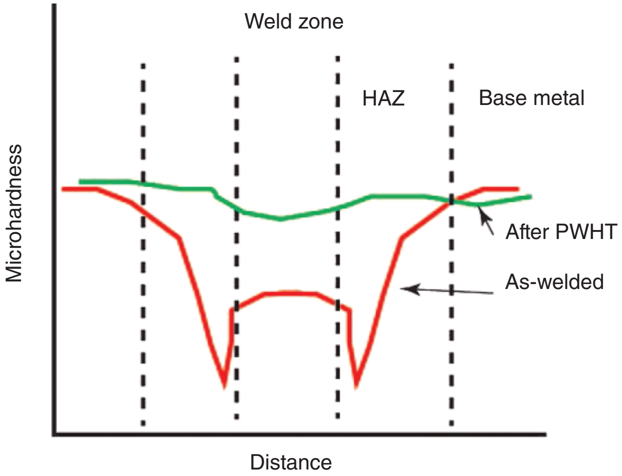

Figure 1.27 Schematic of microhardness profile of a HTA welded by GMAW. Microhardness profile after PWHT.

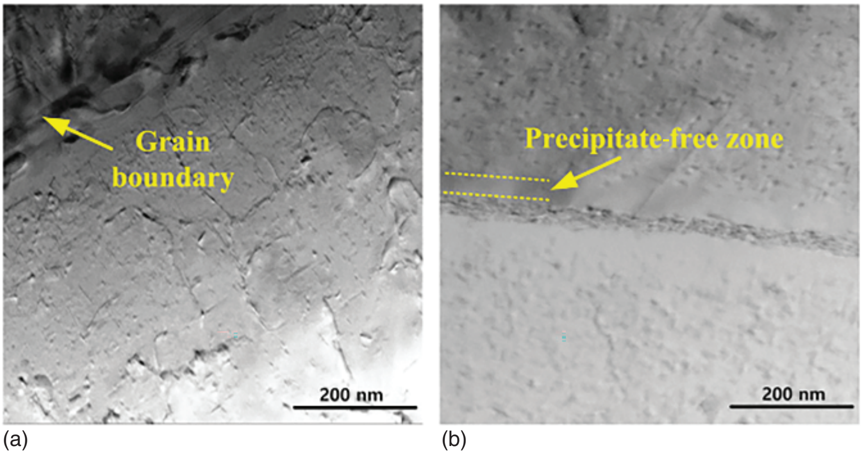

Figure 1.28 (a) FZ of an AA6061 alloy after aging. (b) The FZ after solution treatment and aging. Source: Ref. [67]/with permission of Elsevier.

The response of the FZ and HAZ is not similar to heat treatment. The FZ of Al welds is usually in the solution-treated state while the HAZ can be in various conditions, as mentioned. Due to the segregation of the alloying elements in the liquid phase at the final stage of solidification in the FZ, the solid may have insufficient concentration of elements, which makes it hard to respond to aging heat treatment after welding. An aging at proper time and temperature after welding may recover the hardness in the FZ depending on the degree of segregation [65]. Dislocations may also be present in the FZ of the welds. In the transmission electron microscopy (TEM) image of the FZ of a 6061-T6 Al alloy, no precipitate is observed and some dislocations are discernible. By aging after welding, the dislocations disappear and the precipitates appear [66].

As the final inter-dendritic liquid is rich in alloying elements, depending on the alloy type, some crystal phases form at the grain boundaries which are different from the phases that form during aging of the base material. These inter-granular crystals do not contribute to the strength of the weld, and instead, they reduce the degree of supersaturation inside the grains. Figure 1.28a shows the FZ of an AA6061 alloy welded by resistance welding, which is subsequently aged. The crystals in the grain boundary are discernible. Inside the grain, only a partial precipitation is observed, which is due to the insufficient amount of the alloying elements. When the FZ is solution-treated after welding, the interior of the grains is covered by massive amounts of precipitates during age hardening. A narrow region that corresponds to precipitation-free zone is observed around the grain boundaries (Figure 1.28) [67].

Talking about heat-treatable Al alloys, in solid-state welding processes such as FSW, where no solidification occurs, a nugget zone exists where the precipitates are likely to dissolve due to the heat of the friction. The hardness profile after FSW is dependent on the initial heat treatment state of the Al alloy [68]. When the alloy is in O-temper condition, the nugget zone has the highest hardness due to grain refinement (Figure 1.29). When the Al alloy is precipitate-hardened, for instance T6

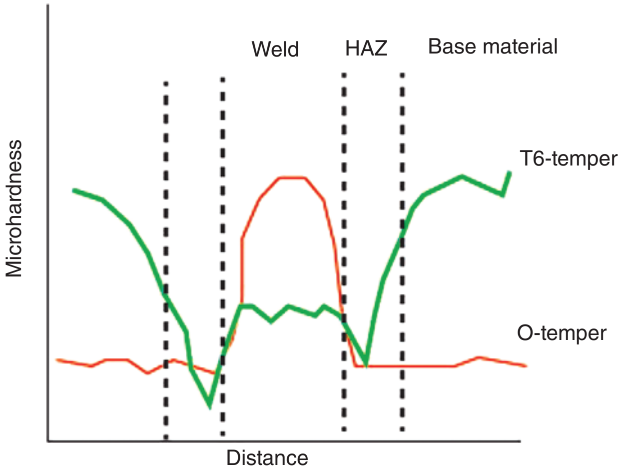

Figure 1.29 Schematic of hardness profile after FSW of O-temper and T6-Temper Al alloy.

condition, the nugget zone has the lowest hardness (Figure 1.29) due to dissolution of the precipitates and elimination of the dislocations. This is despite the finer grains in the nugget zone, because the contribution of the other factors is predominant [68]. So, the main challenge exists for FSW of those Al alloys that are hardened by precipitation. To recover the strength, a fully solutioning and aging treatment is needed in these joints [66]. This kind of heat treatment is not feasible for large structures. Moreover, a large distortion is induced during this heat treatment. Another issue caused by solutioning is the abnormal grain growth in the nugget zone. After FSW, the grains in the nugget zone are refined, which contributes to the weld strength. By subsequent solutioning and abnormal grain growth, a decrease in the strength as well as in the ductility is observed [21]. This decrease is compensated through precipitation by the following aging [69]. The elimination of the solutioning after FSW and only doing artificial aging, the decrease in strength due to grain growth and lower dislocation density is not observed anymore and hence a higher strength is obtained [70].

A detailed characterization of the precipitates and the dislocations needs high-resolution techniques such as TEM. The statistical reliability of this technique depends on the selection basis of the area of the study, as this technique yields useful information in a very small area below 10 μm. Microhardness profile data along with optical microscopy images can be used as bases for selection of the areas to be studied by TEM. The areas with similar hardness and morphology can be represented by choosing a random point for TEM analysis. Useful statistical data of the grains' crystallographic orientation and morphology can be obtained using electron back-scattered diffraction. The morphology of the grains of the weld zone depends on the temperature gradient (G) and the solidification speed (R) (Figure 1.30). The cooling rate (GR) determines the scale of the microstructure and G/R determines the morphology [71]. The extent of each morphology in the FZ depends on the welding process and welding parameters. These are addressed

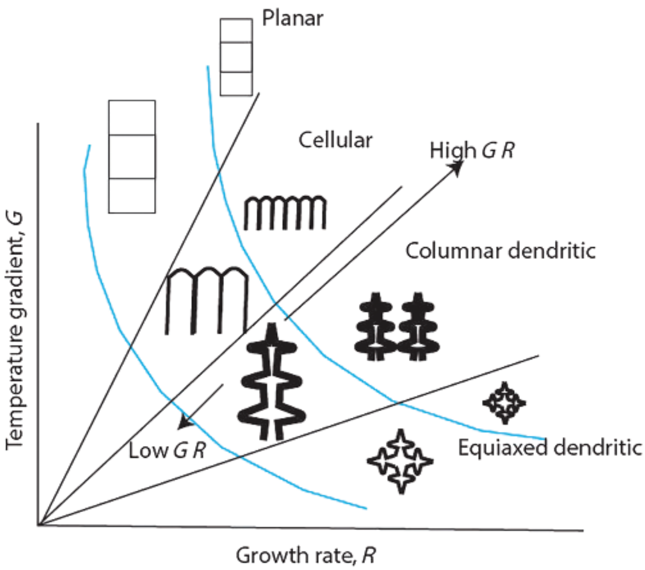

Figure 1.30 Schematic showing the effect of the temperature gradient (*G*) and the solidification speed (*R*) on the morphology and size of the grains in FZ.

in detail in the following chapters for arc welding processes, laser beam welding, resistance welding, and solid-state welding.

The mechanical properties of the weld depend on the microstructure. The microstructure of the FZ is cast, which consists of dendrites or columnar grains. Equiaxed grains may also appear in the weld zone, which is favored over the columnar or dendritic grains. It is shown that the equiaxed grains result in a higher ductility of the weld without any influence on the tensile strength [72]. The fine equiaxed structure provides more grain boundaries, which act as dislocation barriers, causing an increase in the yield strength (σ_y) according to the Hall–Petch equation [73].

$$\sigma_y = \sigma_0 + k.d^{-0.5} \tag{1.17}$$

where σ_0 is the opposite shear stress to the movement of dislocation inside the grain, k is a material constant representing the degree of difficulty to produce grain dislocation, and d is the grain diameter. The grain structure may also affect the mechanical properties through other mechanisms. For example, segregation of the alloying elements that cause hot cracking can also affect the failure mechanism of the joint in loading. Segregation is influenced by the grain structure, as discussed before. Along with the grain size and morphology, other mechanisms such as precipitation hardening, solution hardening, and strain hardening need to be considered in analyzing the mechanical properties of the joint.

In addition to thermal history, the nucleation particles affect the mechanical properties through modification of the solidification structure [74]. The metallographic images of the failed tensile specimens from the weld cross sections

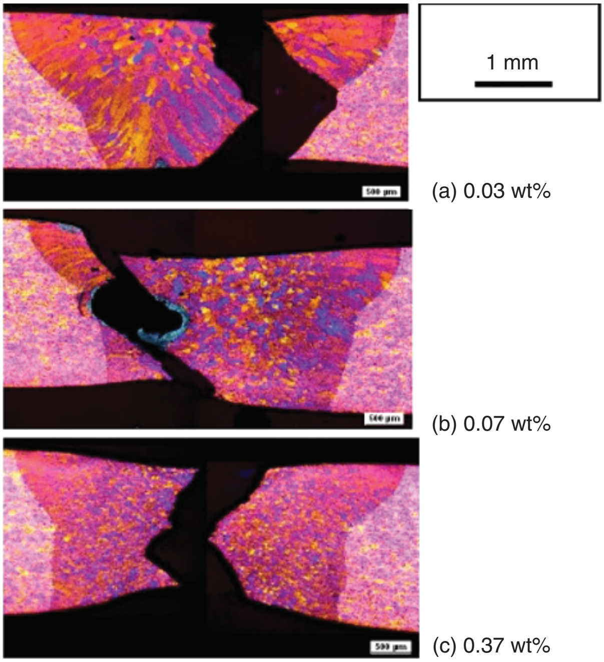

Figure 1.31 Metallographic images of the failed tensile specimens from the weld cross sections of three AA6082Al alloys with three different Ti content welded by laser welding [74]/DVS Media GmbH.

of three AA6082Al alloys with three different Ti content welded by laser welding are shown in Figure 1.31. At low Ti content, the FZ boundary consists of coarse columnar grains, where their boundary act as the fracture site during tensile testing. By 0.07% Ti addition, the fracture occurs along the boundary between the columnar and equiaxed grains. By 0.37% Ti, a full fine-equiaxed grain structure is developed, which promotes higher plastic deformation. The fracture occurs in the middle of the weld zone. The yield strength and ultimate tensile strength (UTS) of three specimens differ slightly, but the elongation of the weld to the fracture is highest in the specimen with the highest amount of Ti. The underlying mechanism by which the failure of the weld is influenced is the segregation and hot cracking caused by the grain structure. The degree of segregation is higher in coarse and columnar grains than the fine and equiaxed ones, as mentioned before. This explains the fracture locations observed in Figure 1.31. The mechanism of grain modification by adding nucleation particles is discussed in more detail in Chapter 2.

The thermal cycle not only influences the microstructure and mechanical properties, but also the distortion and residual stresses during welding. The distortion of Al alloys during welding is higher than steel due to its higher heat conductivity and higher thermal expansion coefficient. There are some basic laws that are practical for avoiding distortion during welding. For fillet welds, two simultaneous welding on both sides reduces the angular distortion. The seam welds, which cause the highest stiffness on the structure, should be performed last. The butt welds should be done before the filler welds [75].

1.4 Welding of Aluminum to Other Metals

A high demand exists for joining of Al to other metals such as steel, magnesium, and titanium, mainly for structural reasons. Welding of Al to copper is also gaining attention for electrical purposes, and hence, Al usage in the energy sector is increasing. The main challenge of welding Al to these materials is the formation of thick intermetallic compounds (IMCs), which are brittle and degrade the mechanical properties of the joint [76]. Usually, the interface is composed of one or more IMC layers at the interface. However, this layer is not always uniform, and its shape and morphology depend on the process and its parameters. The mechanical properties of the joint are highly influenced by the thickness and distribution of IMC as well as the direction of the applied load with respect to the interface [77, 78]. Dependency of the joint strength to the IMC thickness is depicted in Figure 1.32, which shows that while IMCs formation is necessary to establish a joint, its growth needs to be controlled to maintain its thickness in an optimum range.

The thickness of the IMC layer (d_{IMC}) is estimated by the following relationship

$$d_{IMC} = Dt^n \tag{1.18}$$

where D is the diffusion coefficient, t is time, and n is a constant whose value depends on the controlling factor of the growth, diffusion or reaction [79]. In dissimilar joints, the microstructures of the parent materials are not as decisive as the IMC layer, as this layer is the weakest point that controls the mechanical behavior. The mechanisms of IMC formation in fusion welding and solid-state welding processes are discussed in the following chapters.

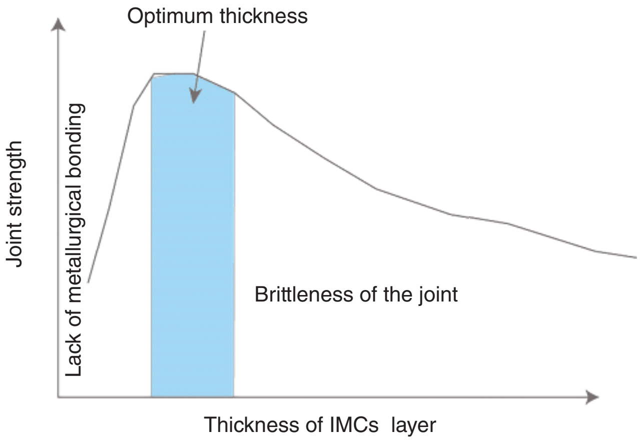

Figure 1.32 Dependency of the joint strength to the IMC thickness.

References

1 Murphy, A., McCune, W., Quinn, D. et al. (2007). The characterisation of friction stir welding process effects on stiffened panel buckling performance. *Thin-Walled Structures* 45 (3): 339–351.

2 Schulze, G. (2004). *Die Metallurgie des Schweißens: Eisenwerkstoffe—Nichteisenmetallische Werkstoffe*. Springer.

3 Dorn, L. (1998). Schweißverhalten von Aluminium und seinen Legierungen. *Materials Science and Engineering Technology* 29 (8): 412–423.

4 Zhang, P., Jia, Z., Yu, Z. et al. (2021). A review on the effect of laser pulse shaping on the microstructure and hot cracking behavior in the welding of alloys. *Optics Laser Technology* 140: 107094.

5 Srikanth, T., Surendran, S., Balaganesan, G. et al. (2017). Response of CMT welded aluminum AA5086-H111 to AA6061-T6 plate with AA4043 filler for ballistic. *Procedia Engineering* 194: 522–528.

6 Gould, J. (2012). Joining aluminum sheet in the automotive industry – a 30 year history. *Welding Journal* 91 (1): 23–34.

7 Sun, T., Franciosa, P., Sokolov, M. et al. (2020). Challenges and opportunities in laser welding of 6xxx high strength aluminium extrusions in automotive battery tray construction. *Procedia CIRP* 94: 565–570.

8 Abioye, T.E., Olanipekun, E., and Anasyida, A.S. (2022). Prediction of the hardness of pulverized glass waste-reinforced aluminium alloy 6061-T6 friction stir welded joint. *International Journal of Engineering Research in Africa* 62: 31–42.

9 Merino, J., Patzelt, A., Steinacher, A. et al. (2017). Ariane 6-Tanks and structures for the new european launcher. *Deutscher Luft- und Raumfahrtkongress*, München. Deutsche Gesellschaft für Luft-und Raumfahrt-Lilienthal-Oberth eV.

10 Cai, C., Shuang, H., Chen, H. et al. (2019). The influences of Ar—He shielding gas mixture on welding characteristics of fiber laser-MIG hybrid welding of aluminum alloy. *Optics & Laser Technology* 113: 37–45.

11 Lee, H.-K., Park, S.-h., and Kang, C.-Y. (2015). Effect of plasma current on surface defects of plasma-MIG welding in cryogenic aluminum alloys. *Journal of Materials Processing Technology* 223: 203–215.

12 Kashaev, N., Ventzke, V., and Çam, G. (2018). Prospects of laser beam welding and friction stir welding processes for aluminum airframe structural applications. *Journal of Manufacturing Processes* 36: 571–600.

13 Hobbacher, A. (2016). *Recommendations for Fatigue Design of Welded Joints and Components*, vol. 47. Springer.

14 Hossain, I., Bhowmik, A., Pattanaik, A. et al. (2024). Computational investigation of plasma arc welding process for aluminium alloys. *Engineering Research Express* 6 (2): 025541.

15 Dobosy, Á., Gáspár, M., and Török, I. (2018). Resistance spot welding of 7075 aluminium alloy. *Proceedings of the Second Vehicle and Automotive Engineering 2: VAE2018*, Miskolc, Hungary. Springer.

16 Dilthey, U. (2006). *Schweißtechnische Fertigungsverfahren 2: Verhalten der Werkstoffe beim Schweißen*. Springer-Verlag.

17 Kovács, J. and Lukács, J. (2022). Investigation of the Possibility for Compensating the HAZ Softening of AA7075-T6. *Periodica Polytechnica Mechanical Engineering* 66 (3): 207–212.

18 Liu, T., Mu, Z., Hu, R. et al. (2019). Sinusoidal oscillating laser welding of 7075 aluminum alloy: hydrodynamics, porosity formation and optimization. *International Journal of Heat and Mass Transfer* 140: 346–358.

19 Enz, J. (2012). *Laserstrahlschweissen von hochfesten Aluminium-Lithium-Legierungen*. Springer.

20 Warner, T. Recently-developed aluminium solutions for aerospace applications. In Materials Science Forum. 2006. *Trans Tech Publications.*

21 Zhang, J., Feng, X.S., Gao, J.S. et al. (2018). Effects of welding parameters and post-heat treatment on mechanical properties of friction stir welded AA2195-T8 Al–Li alloy. *Journal of Materials Science & Technology* 34 (1): 219–227.

22 Avilov, V., Gumenyuk, A., Lammers, M. et al. (2012). PA position full penetration high power laser beam welding of up to 30 mm thick AlMg3 plates using electromagnetic weld pool support. *Science Technology of Welding Joining* 17 (2): 128–133.

23 Tang, G., Chen, H., Yang, X. et al. (2018). Effects of different welding process on the electronic temperature of plasma and weld shape during laser-MIG hybrid welding of A7N01P-T4 aluminum alloy. *Journal of Laser Applications* 30 (2): 022002.

24 Balanovskii, A.E. (2019). A new mechanism of interaction between a welding arc discharge of reverse-polarity direct current and an aluminum surface. *High Temperature* 57: 784–797.

25 Pellone, L., Inmake, G., Hong, K.-M. et al. (2019). Effects of interface gap and shielding gas on the quality of alloy AA6061 fiber laser lap weldings. *Journal of Materials Processing Technology* 268: 201–212.

26 Feng, J., Zhang, P., Yan, H. et al. (2023). Application of laser welding in electric vehicle battery manufacturing: a review. *Coatings* 13 (8): 1313.

27 Kang, Y., Zhan, X.H., and Liu, T. (2019). Effect of welding parameters on porosity distribution of dual laser beam bilateral synchronous welding in 2219 aluminum alloy T-joint. *Journal of Adhesion Science and Technology* 33 (23): 2595–2614.

28 Chen, Q., Ge, H., Yang, C. et al. (2017). Study on pores in ultrasonic-assisted TIG weld of aluminum alloy. *Metals* 7 (2): 53.

29 Ardika, R.D., Triyono, T., and Muhayat, N. (2021). A review porosity in aluminum welding. *Procedia Structural Integrity* 33: 171–180.

30 He, E., Liu, J., Lee, J. et al. (2018). Effect of porosities on tensile properties of laser-welded Al–Li alloy: an experimental and modelling study. *The International Journal of Advanced Manufacturing Technology* 95: 659–671.

31 Yan, S., Zhu, Z., Ma, C. et al. (2019). Porosity formation and its effect on the properties of hybrid laser welded Al alloy joints. *The International Journal of Advanced Manufacturing Technology* 104: 2645–2656.

32 Vyskoč, M., Sahul, M., and Sahul, M. (2018). Effect of shielding gas on the properties of AW 5083 aluminum alloy laser weld joints. *Journal of Materials Engineering and Performance* 27: 2993–3006.

33 Han, X., Yang, Z., Ma, Y. et al. (2020). Porosity distribution and mechanical response of laser-MIG hybrid butt welded 6082-T6 aluminum alloy joint. *Optics & Laser Technology* 132: 106511.

34 Chen, L., Wang, C., Xiong, L. et al. (2020). Microstructural, porosity and mechanical properties of lap joint laser welding for 5182 and 6061 dissimilar aluminum alloys under different place configurations. *Materials & Design* 191: 108625.

35 Miyagi, M., Kawahito, Y., Wang, H. et al. (2018). X-ray phase contrast observation of solidification and hot crack propagation in laser spot welding of aluminum alloy. *Optics Express* 26 (18): 22626–22636.

36 Rappaz, M., Drezet, J.-M., and Gremaud, M. (1999). A new hot-tearing criterion. *Metallurgical and Materials Transactions A* 30: 449–455.

37 Tang, Z. and Vollertsen, F. (2014). Influence of grain refinement on hot cracking in laser welding of aluminum. *Welding in the World, Le Soudage Dans Le Monde* 58: 355–366.

38 Wang, X.J., Lu, F., Wang, H.-P. et al. (2015). Experimental and numerical analysis of solidification cracking behaviour in fibre laser welding of 6013 aluminium alloy. *Science and Technology of Welding & Joining* 20 (1): 58–67.

39 Pumphrey, W.I. and Moore, D.C. (1948). A consideration of the nature of brittleness at temperatures above the solidus in castings and welds in aluminium alloys. *Journal of the Institute of Metals* 75: 235–256.

40 Bielenin, M. (2021). *Prozessstrategien zur Vermeidung von Heißrissen beim Schweißen von Aluminium mit pulsmodulierbaren Laserstrahlquellen*. BoD–Books on Demand.

41 Kubo, K. and Pehlke, R.D. (1985). Mathematical modeling of porosity formation in solidification. *Metallurgical and Materials Transactions B* 16: 359–366.

42 Kou, S. (2003). *Welding Metallurgy*, 223–225. John Wiley & Sons.

43 Kou, S., Firouzdor, V., and Haygood, I.W. (2011). Hot cracking in welds of aluminum and magnesium alloys. *Materials Science Engineering* 3–23.

44 Jennings, P.H. (1949). *Hot-shortness of Some High-purity Alloys in the Systems Aluminium–Copper–Silicon and Aluminium–Magnesium–Silicon*. Aluminium Development Association.

45 Coniglio, N. and Cross, C.E. (2009). Mechanisms for solidification crack initiation and growth in aluminum welding. *Metallurgical and Materials Transactions A* 40: 2718–2728.

46 Tian, Y., Robson, J.D., Riekehr, S. et al. (2016). Process optimization of dual-laser beam welding of advanced Al–Li alloys through hot cracking susceptibility modeling. *Metallurgical Materials Transactions A* 47: 3533–3544.

47 Hagenlocher, C., Weller, D., Weber, R. et al. (2019). Analytical description of the influence of the welding parameters on the hot cracking susceptibility of laser beam welds in aluminum alloys. *Metallurgical and Materials Transactions A* 50: 5174–5180.

48 Von Witzendorff, P., Kaierle, S., Suttmann, O. et al. (2015). In situ observation of solidification conditions in pulsed laser welding of AL6082 aluminum alloys to evaluate their impact on hot cracking susceptibility. *Metallurgical and Materials Transactions A* 46: 1678–1688.

49 Hagenlocher, C., Stritt, P., Weber, R. et al. (2018). Strain signatures associated to the formation of hot cracks during laser beam welding of aluminum alloys. *Optics and Lasers in Engineering* 100: 131–140.

50 Coniglio, N., Cross, C.E., Michael, T. et al. (2008). Defining a critical weld dilution to avoid solidification cracking in aluminum. *Welding Journal* 87 (8): 237s–247s.

51 Wei, H., Chen, J.S., Wang, H.-P. et al. (2016). Thermomechanical numerical analysis of hot cracking during laser welding of 6XXX aluminum alloys. *Journal of Laser Applications* 28 (2): 022405.

52 Norouzian, M., Elahi, M.A., and Plapper, P. (2023). A review: suppression of the solidification cracks in the laser welding process by controlling the grain structure and chemical compositions. *Journal of Advanced Joining Processes* 7 (9): 100139.

53 Hagenlocher, C., Weller, D., Weber, R. et al. (2019). Reduction of the hot cracking susceptibility of laser beam welds in AlMgSi alloys by increasing the number of grain boundaries. *Science and Technology of Welding & Joining* 24 (4): 313–319.

54 Easton, M.A., Grandfield, J., John, S., D. et al. (2006). The effect of grain refinement and cooling rate on the hot tearing of wrought aluminium alloys. *Materials Science Forum* 519–521: 1675–1680. Trans Tech Publications.

55 Soysal, T. (2021). A criterion to find crack-resistant aluminium alloys to avoid solidification cracking. *Science and Technology of Welding & Joining* 26 (2): 99–105.

56 Liu, J. and Kou, S. (2016). Crack susceptibility of binary aluminum alloys during solidification. *Acta Materialia* 110: 84–94.

57 Liu, J. and Kou, S. (2017). Susceptibility of ternary aluminum alloys to cracking during solidification. *Acta Materialia* 125: 513–523.

58 Liu, J. and Kou, S. (2015). Effect of diffusion on susceptibility to cracking during solidification. *Acta Materialia* 100: 359–368.

59 Malekshahi Beiranvand, Z., Ghaini, F.M., Naffakh-Moosavy, H. et al. (2019). An analytical model for prediction of solidification cracking susceptibility in aluminum alloys taking into account the effect of solidification rate. *Metallurgical Transactions A* 50: 2835–2846.

60 Holzer, M., Hofmann, K., Mann, V. et al. (2016). Change of hot cracking susceptibility in welding of high strength aluminum alloy AA 7075. *Physics Procedia* 83: 463–471.

61 Deng, A., Chen, H., Zhang, Y. et al. (2023). Prediction of the influence of welding metal composition on solidification cracking of laser welded aluminum alloy. *Materials Today Communications* 35: 105556.

62 Wan, Z., Meng, D., Zhao, Y. et al. (2022). Improvement in tensile properties of 2219-T8 aluminum alloy TIG welding joint by PMZ local properties and stress distribution. *Journal of Manufacturing Processes* 839: 142863.

63 Jula, M., Dehmolaei, R., and Ranjbar, K. (2023). Softening, hardening, and precipitation evolution of the AA6082-T651 heat-affected zone caused by thermal cycles during and after welding. *Metals and Materials International* 29 (12): 3664–3678.

64 Pérez, J.S., Ambriz, R.R., Curiel López, F.F. et al. (2016). Recovery of mechanical properties of a 6061-T6 aluminum weld by heat treatment after welding. *Metallurgical and Materials Transactions A* 47: 3412–3422.

65 Cheng, J., Song, G., Zhang, X. et al. (2021). Review of techniques for improvement of softening behavior of age-hardening aluminum alloy welded joints. *Materials (Basel)* 14 (19): 5804.

66 Jie, Y., Wang, G., Li, S.-k. et al. (2019). Effect of post-weld heat treatment on microstructure and mechanical properties of welded joints of 6061-T6 aluminum alloy. *Transactions of Nonferrous Metals Society of China* 29 (10): 2035–2046.

67 Zhang, Y., Li, H., Li, Z. et al. (2021). Quantitative analysis of the solute redistribution and precipitate of Al–Mg–Si series alloys resistance spot welds after post–weld heat treatment. *Journal of Materials Research and Technology* 15: 5906–5919.

68 Chen, Y., Liu, H., and Feng, J. (2006). Friction stir welding characteristics of different heat-treated-state 2219 aluminum alloy plates. *Materials Science and Engineering: A* 420 (1–2): 21–25.

69 Aydın, H., Bayram, A., and Durgun, I. (2010). The effect of post-weld heat treatment on the mechanical properties of 2024-T4 friction stir-welded joints. *Materials & Design* 31 (5): 2568–2577.

70 Elangovan, K. and Balasubramanian, V. (2008). Influences of post-weld heat treatment on tensile properties of friction stir-welded AA6061 aluminum alloy joints. *Materials Characterization* 59 (9): 1168–1177.

71 Geng, S., Jiang, P., Shao, X. et al. (2020). Heat transfer and fluid flow and their effects on the solidification microstructure in full-penetration laser welding of aluminum sheet. *Journal of Materials Science & Technology* 46: 50–63.

72 Wang, L., Gao, M., Zhang, C. et al. (2016). Effect of beam oscillating pattern on weld characterization of laser welding of AA6061-T6 aluminum alloy. *Materials & Design* 108: 707–717.

73 Saifudin, S., Muhayat, N., Surojo, E. et al. (2022). Mitigation of porosity and residual stress on car body aluminum alloy vibration welding: a systematic literature review. *Automotive Experiences* 5 (3): 477–493.

74 Tang, Z., Schempp, P., Seefeld, T. et al. (2011). *Kornfeinung beim WIG-und Laserstrahlschweißen von Aluminiumlegierungen*. DVS-Verlag.

75 Nölle, P. (2011). Verzugarmes Schweißen von Aluminiumwerkstoffen. *Lightweight Design* 4 (2): 58–63.

76 Beygi, R., Kazeminezhad, M., and Kokabi, A.H. (2014). Microstructural evolution and fracture behavior of friction-stir-welded Al—Cu laminated composites. *Metallurgical and Materials Transactions A* 45: 361–370.

77 Beygi, R., Talkhabi, A.A., Mehrizi, M.Z. et al. (2023). A novel lap-butt joint design for FSW of aluminum to steel in Tee-configuration: joining mechanism, intermetallic formation, and fracture behavior. *Metals* 13 (6): 1027.

78 Beygi, R., Carbas, R.J.C., Marques, E.A.S. et al. (2023). Mechanism of toughness enhancement of brittle fracture by intermittent η-intermetallic in Al/Cu joint made by FSW. *Materials Science and Engineering A* 145907.

79 Springer, H., Kostka, A., Payton, E. et al. (2011). On the formation and growth of intermetallic phases during interdiffusion between low-carbon steel and aluminum alloys. *Acta Materialia* 59 (4): 1586–1600.